Hybrid perovskites: intrinsic multi-valley and multi-bandgap absorption for efficient solar cells

Jacky Even, Laurent Pedesseau, Claudine Katan

Title: Hybrid perovskites: intrinsic multi-valley and multi-bandgap absorption for efficient solar cells

Authors: J. Even[1]*, L. Pedesseau[1], C. Katan[2]

Affiliations:

[1]Université Européenne de Bretagne, INSA FOTON UMR 6082, 35708 Rennes, France.
[2]CNRS, Institut des Sciences Chimiques de Rennes UMR6226, 35042 Rennes, France
*Correspondence to: jacky.even@insa-rennes.fr

Abstract: Solution-processable metal-halide perovskites recently opened a new route towards low-cost manufacture of solar cells, and currently meso-superstructured solar cells and solid thin-film planar hetero-junction show record efficiencies. Based on group theory analyses combined to state of the art DFT calculations, we demonstrate that such hybrid perovskites are natural multi-bandgap and multi-valley materials, leading to a broad absorption across the solar spectrum and attractive charge transport properties. Our results further suggest that polymorphism may lead to exciton screening and reduced carrier mobility. $CH_3NH_3SnI_{3-x}Br_x$ is proposed as an alternative to circumvent polymorphism at room temperature and toxicity, and is likely to offer environmental friendly materials for photovoltaics. We believe that the past research effort invested in the field of *conventional semiconductors* provides forefront concepts and tools to unravel our understanding of this new class of materials.

One Sentence Summary: The broad absorption among the solar spectrum of hybrid 3D perovskites is related to the intrinsic multi-bandgap and multi-valley nature of their electronic band edge states.

Main Text:

Based on fundamental physical laws, the Shockley-Queisser limit is recognized to be a theoretical limit of the efficiency of an ideal single p-n junction solar cell (1). To date, the highest efficiencies of photovoltaic (PV) conversion attained for heterojunctions remains below this limit and alternative strategies have been explored such as concentrated multi-junction PV cells (2,3). The latter undeniably afford upmost solar-to-electrical power conversion efficiencies (2) but at the expense of elaborate and expensive growth modus operandi. Conversely, the tremendous research effort conducted during the last year on solution-processable metal-halide perovskites has opened a new route towards low-cost manufacture of solar cells. First used as the sensitizer in conventional dye sensitized solar cells (4-6), thanks to their broad absorption across the solar spectrum, their attractive charge transport properties allowed to achieve recently Meso-Superstructured Solar Cell (MSSC) and solid thin-film planar heterojunctions with record efficiencies up to 15% (7-15). Attention has mainly focused on the methylammonium lead-iodide perovskite ($CH_3NH_3PbX_3$, X=I) that affords good light harvesting and ambipolar transport abilities (15). Halogen substitution ($X_3=I_{3-x}Cl_x$ or $I_{3-x}Br_x$) has shown to provide improved transport properties and cell stability while preserving good performances including low fundamental energy losses (5,11-13). Despite this breakthrough in PV-technology, fundamental understanding of the photophysics of these perovskites remains scarce (14-16). In particular, the origin of the favorable light absorption over the visible to near-IR range is still unanswered in spite of a couple of recent theoretical investigations based on density functional theory (DFT) (17-23). Nonetheless, DFT calculations have already evidenced the importance of spin-orbit coupling (SOC) and polymorphism (24) on the electronic band structure of $CH_3NH_3PbI_3$ and related compounds (17,18). Thus, polymorphism is another issue for PV cells operating at room

temperature (RT). Moreover, the high percentage of lead might be a problem for future development regarding European Directives on the use of hazardous substances in electrical and electronic equipment (25). Replacement of lead by tin is an option that may also solve the polymorphism problem happening in iodide-based perovskites (18,24).

This prompts us to theoretically investigate the absorption features of the metal-halide perovskites: $CH_3NH_3MX_3$, X=I, Br, Cl and M=Pb, Sn, Ge. Based on group theory analyses combined to state of the art DFT calculations, the present work aims to demonstrate that such hybrid perovskites are natural multi-bandgap and multi-valley materials. Polymorphism, metal substitution and excitonic effects are analyzed. Computational details are provided as supplementary materials.

At room temperature, the linear absorption spectrum of $CH_3NH_3PbI_3$ shows two absorption peaks located at 760 and 480 nm (14,15). Whereas the low energy peak was attributed to the direct bandgap transition from the valence band (VB) maximum to the conduction band (CB) minimum, the origin of the high energy peak remained unresolved (15). Interestingly, recent calculations, performed without SOC and within the Random-Phase Approximation (RPA), of the imaginary part of the dielectric function for the high temperature cubic phase of $CH_3NH_3PbI_3$ evidenced the onset of a primary and a secondary absorption related to the R and M points of the first brillouin zone (BZ) of the Pm3m space group, respectively (18). A first insight in these optical features can be gained from group theory and by considering the giant spin-orbit effect on the CB evidenced in both 3D and 2D lead-based hybrid perovskites (17,18,26). The symmetry analysis of the electronic states at R and M in the simple and double group allows identifying the optically allowed transitions. The simple group T_{1u} vectorial representation of the CB at R is splitted in a doubly degenerated $E_{1/2u}$ (spin-orbit split-off states)

and a fourfold degenerated $F_{3/2u}$ state (fig. S1). The ground state isotropic optical transition is thus predicted at R between doubly degenerated $E_{1/2g}$ VB and $E_{1/2u}$ CB states depicted figure 1 for the calculated band structure. Complete diagrams with and without SOC are provided as supplementary materials (fig. S2, S3). At R, a series of other transitions are optically allowed, the lowest in energy corresponding to two secondary transitions $E_{1/2g} \rightarrow F_{3/2u}$ and $F_{3/2g} \rightarrow E_{1/2u}$. However, given the calculated band structure (fig. 1) and symmetry (fig. S1), the transition between the doubly degenerated $E_{1/2g}$ VB and $E_{1/2u}$ CB states at M is optically allowed, energetically lower than secondary transitions at R, transverse electric (TE), and may be at the origin of the peak observed at 480nm. In fact, the relative weight of the energy parameter quantifying the optical matrix elements, defined by $\frac{2}{m_e}|\langle \psi_{CB}|-i\hbar\nabla|\psi_{VB}\rangle|^2$ and computed for the low-energy transitions at R and M (table S3,S4), evidence larger weights for the latter, thanks to threefold contributions stemming from M, and an upwards energy shift of about 1eV, consistently with experimental findings. The threefold contribution can be intuited from the Fermi surface plotted in the first BZ close to the top of the VB (Fig. 1). Moreover, the different optically allowed transitions have sizeable matrix elements disclosing the multi-bandgap nature at the origin of the visible to near-IR light-harvesting capabilities of $CH_3NH_3PbI_3$ (see also additional text in the supplementary materials).

Next, the Fermi surface (Fig. 1) reveals clear connection between R and M along the edges of the BZ. While the BZ valleys are located around R, M correspond to saddle points. This suggests that, in reciprocal space, carriers generated by optical absorption at M and all along the M→R paths at various wavelengths (fig. 1) can flow easily towards R. The relaxation process may be assisted by acoustic phonons. Contrarily, one expects that some of the carriers generated by the secondary optical transitions at R may be trapped in the $F_{3/2u}$ (CB) and $F_{3/2g}$ (VB) states.

Further relaxation $F_{3/2g} \rightarrow E_{1/2g}$ (holes) and $F_{3/2u} \rightarrow E_{1/2u}$ (electrons) may occur by optical phonons assisted relaxations, provided that the energy conservation rule is exactly fulfilled. Such a "phonon bottleneck" is well known in the case of carrier injection in semiconductor quantum dots (27,28). However, in quantum dots, carrier assisted (Auger relaxation) is the dominant effect in the high injection regime, yielding very fast carrier relaxation. A similar hot hole cooling (intra-band process) from $F_{3/2g}$ to $F_{1/2g}$ is consistent with the relaxation after optical excitation reported for $CH_3NH_3PbI_3$ (15).

Similar results are obtained by halogen substitution, as illustrated for the cubic Pm3m phase of $CH_3NH_3PbCl_3$ (fig. S4, table S5,S6), with a larger bandgap and a larger splitting between primary (R) and secondary (M) optical transitions. This prompts a short comment on calculated bandgaps. Indeed, while it is well known that DFT bandgaps should be corrected for many-body effects to be compared with optical bandgaps (see supplementary materials), the importance of SOC for lead-based perovskites prevents systematic implementation of GW self-energy corrections. Nevertheless, the systematic bandgap increase observed upon halogen substitution (I, Br, Cl) is well accounted for within DFT both with and without SOC (table S1) and we carry on with chlorine to investigate metal substitution. Optical absorption spectra of $CH_3NH_3MCl_3$ (M=Pb, Sn, Ge) in their high temperature Pm3m cubic phases (Fig. 2) illustrate further the importance of SOC effects which are mandatory to recover the correct bandgap ranking (18). As expected, SOC induces only slight changes for germanium-based perovskites (see also fig. S9 compared to fig. S7,S10). These calculated optical absorption spectra (Fig. 2B) suggest attractive light-harvesting abilities for the cubic phases of both $CH_3NH_3SnCl_3$ and $CH_3NH_3GeCl_3$, i.e. comparable to those obtained for the room temperature cubic phase of $CH_3NH_3PbCl_3$. We may notice that the large experimental bandgaps obtained with X=Cl, of 3.1

(29) and 3.7(30) eV for M=Pb and M=Sn respectively, are not favorable for PV technologies based on pure materials. On the other hand, with X=I and M=Sn, the experimental bandgap at room temperature drops to 1.2 eV (24) close to the 1.5 eV measured for M=Pb (4). While the possibility to build solid solutions of $CH_3NH_3SnI_{3-x}Cl_x$ was unsuccessful (31) $CH_3NH_3SnI_{3-x}Br_x$ may be an interesting alternative. In fact, for its all-bromide analogue, the experimental bandgap amounts to 2.15eV (30), and both tin-based hybrid perovskites with X=Br and I are reported to crystallize in a cubic phase at room temperature (30,31). Such solid solution may also provide a way to circumvent problems related to polymorphism (18,24,30-32).

This raises the question about the possible issues of polymorphism. In fact, $CH_3NH_3MX_3$ compounds have been reported to undergo phase transitions and do not systematically crystallize in a room temperature cubic phase. For example, the room temperature crystal structure of $CH_3NH_3MI_3$ (M=Pb and Sn) have recently been reinvestigated and shown to be tetragonal (I4cm and P4mm respectively) (24). In addition to the calculated band structures (including SOC) described earlier (18,24), we investigated complementary available crystal structures reported for $CH_3NH_3MX_3$ compounds (fig. S4-S11). To illustrate the effect of polymorphism, figure 3 shows the computed absorption spectra for light polarized perpendicular and parallel to the tetragonal axis of $CH_3NH_3MI_3$ (M= Pb, Sn), and the corresponding spectrum for cubic phase for the lead-based perovskite. Band to band optical absorptions are indeed anisotropic in the tetragonal I4cm phase, but remain comparable to those obtained for the cubic phase. A slight anisotropy of the real parts of the dielectric tensor diagonal components is also predicted: $\varepsilon_{\infty 11}$=5.4 and $\varepsilon_{\infty 33}$=5.7. Such simulations capture the effects of cell strain, ferroelectric symmetry breaking and inorganic lattice deformation. The effect of organic cation's orientation, which does not account for cell strain, has recently been studied by Brivio et al (19). When the electric dipole of the cation is

oriented along [100], similar ferroelectric symmetry breaking and anisotropy of the real part of the dielectric tensor components are obtained, namely: $\varepsilon_{\infty 11}$= 6.29, $\varepsilon_{\infty 22}$= 5.89, $\varepsilon_{\infty 33}$= 5.75 (19). The symmetry breaking induces LO-TO phonon splitting and a large difference between ε_∞ and the static tensor ε_s, the latter amounting to ε_{s11}= 22.39, ε_{s22}= 27.65, ε_{s33}= 17.97 for [100] electric dipole orientation (19). This induces a screening of the electron-hole interaction (fig. S12), thereby reducing the excitonic enhancement of the absorption at the bandgap energy. Because the room temperature phase of $CH_3NH_3PbCl_3$ is known to be cubic, such an effect should not occur and the enhanced absorption due to excitonic effects evidenced by BSE calculations (fig. S13) should be preserved. (35) This may be a further reason for building mixed-halides perovskites based on chlorine and iodine (12).

We can further speculate that polymorphism and the existence of a polar and strained room temperature phase for $CH_3NH_3PbI_3$, may have a dramatic effect on carrier mobility. Indeed, for conventional semiconductors it is known that additional intra-valley mechanisms, such as Fröhlich electron–optical phonon interactions, exist for carrier-phonon scattering in polar materials. Moreover, from our results we may also expect that inter-valley mechanisms, involving zone edge phonons, play a significant role. In the cubic phase, carrier valleys after scattering lie in the same BZ (M→M) or in adjacent ones. Enhancement of the electron-hole diffusion lengths reported for $CH_3NH_3PbI_{3-x}Cl_x$ as compared to $CH_3NH_3PbI_3$ (14) suggests that most of the carrier-phonon processes are avoided when the cubic to tetragonal phase transition is bypassed at room temperature through alloying.

In summary, this work indicates that the broad light-harvesting abilities of the inorganic-organic family of perovskites $CH_3NH_3MX_3$, recently used for high-performance solar cells, is a direct consequence of their intrinsic multi-bandgap and multi-valley nature. In some sense, they

can be thought as natural multi-junction. Inspection of polymorphism suggests that while it should little affect optical absorption, except for dielectric screening in polar phases, it may have dramatic effects on carrier mobilities. Alloys built from mixed-halides, such as $CH_3NH_3PbI_{3-x}Cl_x$, may allow to retain room temperature cubic phases, thus avoiding some of the carrier-phonon relaxation processes which are detrimental to electron-hole diffusion lengths. Tin based mixed-halides ($CH_3NH_3SnI_{3-x}Br_x$) are also suggested as a less toxic but potentially efficient alternative to lead-based perovskites. While fabrication of high-performing PV cells from hybrid perovskites made an outstanding breakthrough in a couple of month, numerous fundamental questions remain open (13-16). We believe that the past research effort invested in the field of *conventional semiconductors* provides forefront concepts and tools to unravel our understanding of this new class of materials.

References and Notes:

1. W. Shockley, H. J. Queisser, *J. Appl. Phys.*, **32**, 510-519 (1961).

2. M. A. Green, K. Emery, Y. Hishikawa, W. Warta, E.D. Dunlop, *Prog. Photovolt: Res. Appl.*, **21**, 827–837 (2013).

3. D.J. Friedman, *Current Opinion in Solid State and Materials Science*, **14**, 131-138 (2010).

4. A. Kojima, K. Teshima, Y. Shirai, T. Miyasaka, *J. Am. Chem. Soc.*, **131**, 6050-6051 (2009).

5. M. M. Lee, J. Teuscher, T. Miyasaka, T. N. Murakami, H. J. Snaith, *Science*, **338**, 643-647 (2012).

6. H-S. Kim, C-R. Lee, J-H Im, K-B. Lee, T. Moehl, A. Marchioro, S-J. Moon, R. Humphry-Baker, J-H. Yum, J. E. Moser, M. Grätzel, N-G. Park, *Sci. Rep.*, **2**, 591-1-591-7 (2012).

7. J. H. Heo, S. H. Im, J. H. Noh, T.N. Mandal, C.S. Lim, J.A. Chang, Y.H. Lee, H.J. Kim, A. Sarkar, M.K. Nazeeruddin, M. Gratzel, S. I. Seok, *Nature Photonics*, **7**, 486-491 (2013).

8. J. Burschka, N. Pellet, S.J. Moon, R. Humphry-Baker, P.Gao, M. K. Nazeeruddin, M. Grätzel, *Nature*, **499**, 316-319 (2013).

9. H-S Kim, I. Mora-Sero, V. Gonzalez-Pedro, F. Fabregat-Santiago, E. J. Juarez-Perez, N-G Park, J. Bisquert, *Nature Comm.*, **4**, 2242 (2013).

10. N. G. Park, *J. Phys Chem. Lett.*, **4**, 2423-2429 (2013).

11. J. H. Noh, S. H. Im, J. H. Heo, T. N. Mandal, S. I. Seok, *Nano Lett.*, **13**, 1764-1769 (2013).

12. M. Liu, M. B. Johnston, H. J. Snaith, *Nature*, **501**, 395-398 (2013).

13. H. Snaith, *J. Phys Chem. Lett.*, **4**, 3623-3630 (2013).

14. S. D. Stranks, G. E. Eperon, G. Grancini, C. Menelaou, M. J. P. Alcocer, T. Leijtens, L. M. Herz, A. Petrozza, H. J. Snaith, *Science*, **342**, 341-344 (2013).

15. G. Xing, N. Mathews, S. Sun, S. S. Lim, Y. M. Lam, M. Grätzel, S. Mhaisalkar, T. C. Sum, *Science*, **342**, 344-347 (2013).

16. M. Antonietta, J. C. Hummelen, *Nature Mater.*, **12**, 1087-1089 (2013).

17. J. Even, L. Pedesseau, J.-M. Jancu, C. Katan, *J. Phys. Chem. Lett.*, **4**, 2999-3005 (2013).

18. J. Even, L. Pedesseau, J.-M. Jancu, C. Katan, *Phys. Status Solidi RRL*, (2013), DOI 10.1002/pssr.201308183

19. F. Brivio, A. B. Walker, A. Walsh, *Appl. Phys. Lett. Mat.*, **1**, 042111-1-042111-5 (2013).

20. T. Baikie, Y. Fang, J. M. Kadro, M. Schreyer, F. Wei, S. G. Mhaisalkar, M. Graetzel, T. J. White, *J. Mater. Chem. A*, **1**, 5628-5641 (2013).

21. S. Colella, E. Mosconi, P. Fedeli, A. Listorti, F. Gazza, F. Orlandi, P. Ferro, T. Besagni, A. Rizzo, G. Calestani, G. Gigli, F. De Angelis, R. Mosca, *Chem. Mater.*, **25**, 4613-4618 (2013).

22. E. Mosconi, A. Amat, Md. K. Nazeeruddin, M. Grätzel, F. De Angelis, *J. Phys. Chem. C*, **117**, 13902-13913 (2013).

23. G. Giorgi, J.-I. Fujisawa, H. Segawa, K. Yamashita, *J. Phys. Chem. Lett.*, **4**, 4213-4216 (2013).

24. C. C. Stoumpos, C. D. Malliakas, M. G. Kanatzidis, *Inorg. Chem.*, **52**, 9019-9038 (2013).

25. M. Saurat, M. Ritthoff, Position Paper, Wuppertal Institute for Climate, Environment and Energy, May 2010

26. J. Even, L. Pedesseau, M.-A. Dupertuis, J.-M. Jancu, C. Katan, *Phys. Rev. B*, **86**, 205301-1-205301-4 (2012).

27. R. Ferreira, G. Bastard, *Appl. Phys. Lett.*, **74**, 2818-2820 (1999).

28. P. Miska, J. Even, X. Marie, O. Dehaese, *Appl. Phys. Lett.*, **94**, 061916-1-061916-3 (2009).

29. N. Kitazawa, Y. Watanabe, Y. Nakamura, *J. Mat. Sci.*, **37**, 3585-3587 (2002).

30. F. Chiarella, A. Zappettini, F. Licci, *Phys. Rev. B*, **77**, 045129-1-045129-6 (2008).

31. K. Yamada, K. Nakada, Y. Takeuchi, K. Nawa, Y.Yamane, *Bull. Chem. Soc. Jpn*, **84**, 926-932 (2011).

32. K. Yamada, Y. Kuranaga, K. Ueda, S. Goto, T. Okuda, Y. Furukawa, *Bull. Chem. Soc. Jpn.*, **71**, 127-134 (1998).

33. Here we may notice that excitonic effects for the secondary transition at M (fig. 1) are expected to be vanishing as a consequence of its saddle point nature.

Acknowledgments: This work was performed using HPC resources from GENCI-CINES/IDRIS grant 2013-c2013096724. The work is supported by Agence Nationale pour la Recherche (PEROCAI project ANR-10-04).

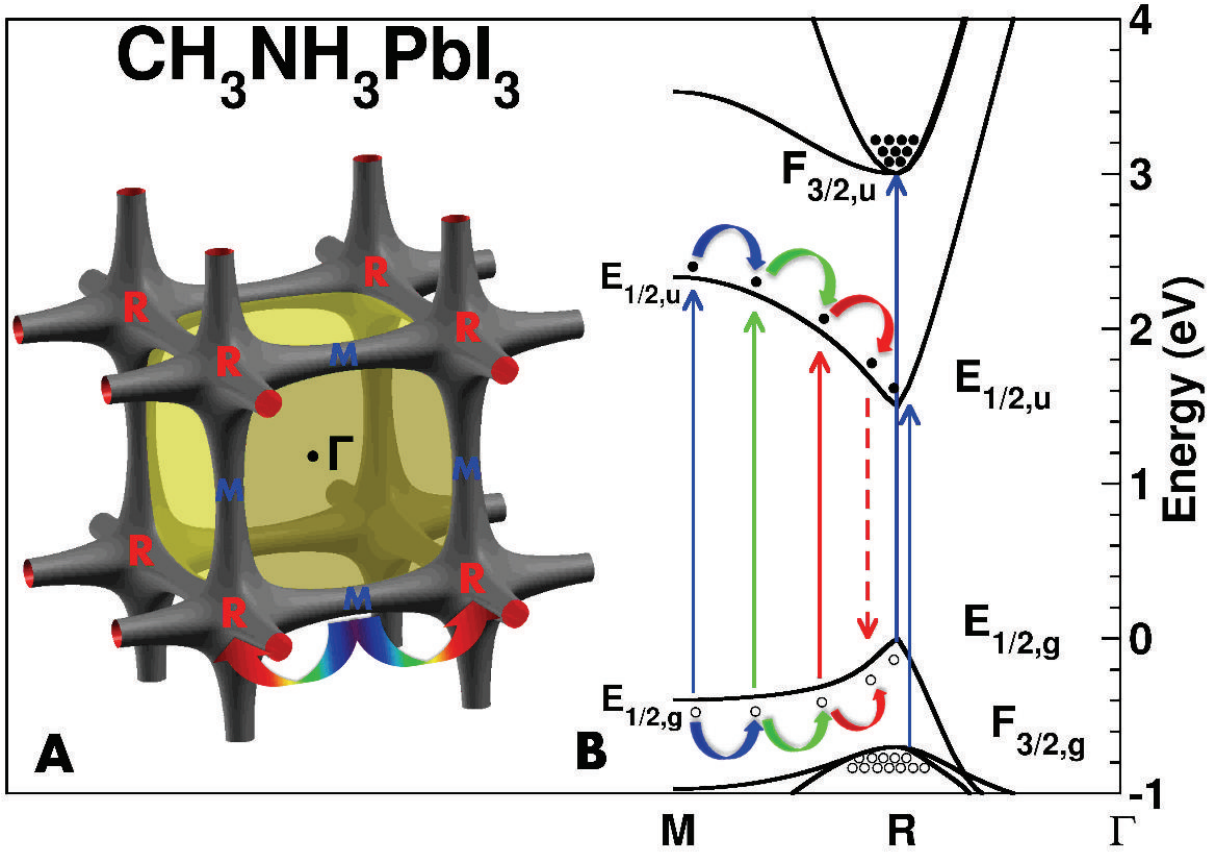

Fig. 1. (A) Fermi surface (E=-0.5eV) in the first BZ. R and M are connected along the edges, showing that M are saddle points. **(B)** Electronic band diagram of the high temperature Pm3m cubic phase of $CH_3NH_3PbI_3$ with SOC; an upward energy shift of 1.4eV has been applied to match the experimental bandgap value at R.

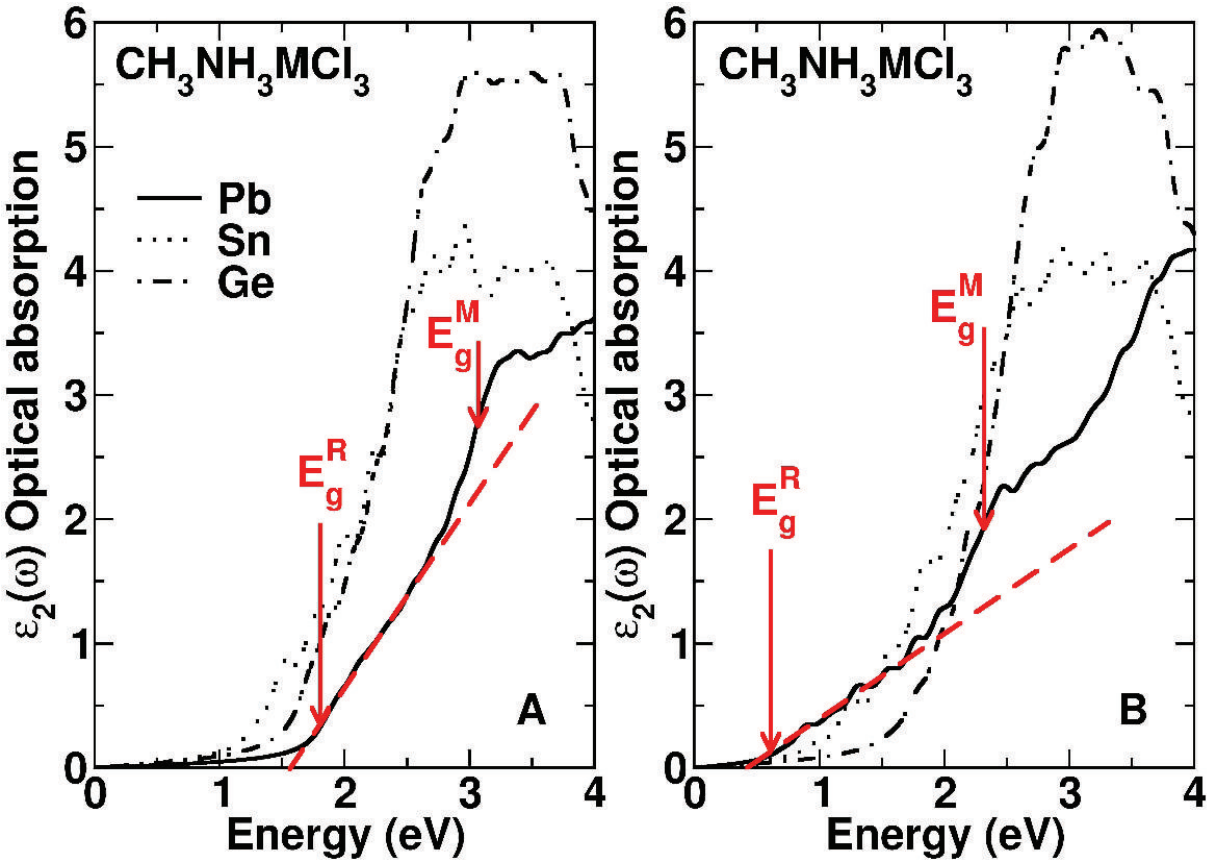

Fig. 2. Comparison of the absorption spectra of $CH_3NH_3MCl_3$ (M=Pb, Sn, Ge) for the high temperature cubic phases without **(A)** and with **(B)** SOC. Onsets of optical absorption at R and M are indicated for $CH_3NH_3PbCl_3$.

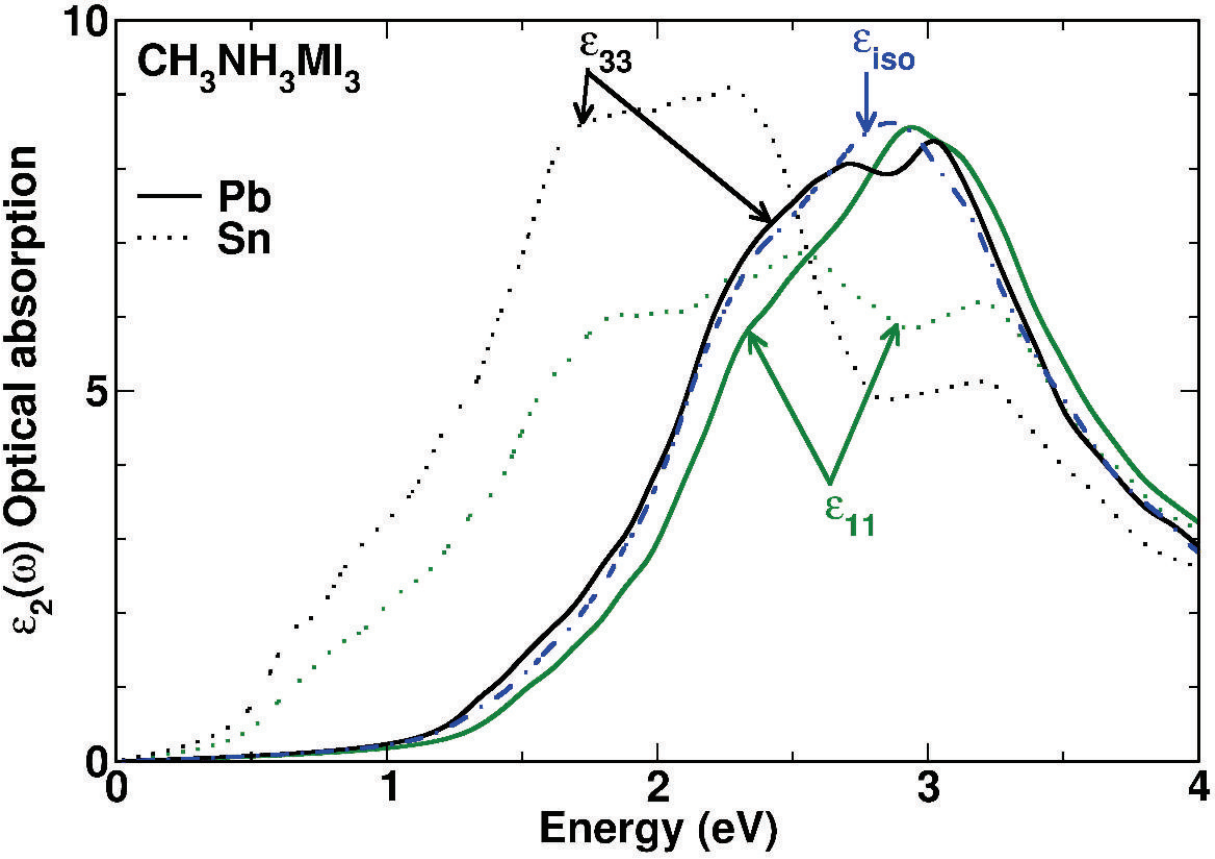

Fig. 3. Comparison of the optical absorption spectra with light polarized perpendicular (ε_{11}) or parallel (ε_{33}) to the tetragonal axis of $CH_3NH_3MI_3$ (M=Pb, Sn) for the I4cm phases, without SOC. The isotropic optical absorption (ε_{iso}) is given for comparison in the case of the cubic phase for M=Pb.

Supplementary Materials:

Materials and Methods

Supplementary Text

Figures S1-S13

Tables S1-S6

References (*1-44*)

Materials and Methods

The first principles calculations were carried out using the DFT implementation available in the ABINIT pseudo-potential package (34) with LDA or GGA (35) for exchange-correlation. Relativistic, norm-conserving, separable, dual-space Gaussian-type pseudopotentials of Goedecker, Teter and Hutter (HGH) have been used for all atoms in order to include the spin-orbit coupling (SOC) (36). The electronic wave-functions are expanded onto a plane-wave basis set with an energy cut-off of 680 eV. This level of theory has already been checked, especially against all-electron computations and for the respective number of core and valence electrons in our previous works (17,18,26,37). Optical absorption spectra were computed from the imaginary part ($\varepsilon_2(\omega)$) of the macroscopic dielectric function (38) with a 16x16x16 grid except for the cubic phase for which a 24x24x24 grid was chosen. The Bethe-Salpeter equation (BSE) was solved for the cubic phase with a 12x12x12 grid (18,38).

It has been previously shown (17) that, close to the bandgap, the band structure of hybrid perovskites is accurately reproduced by replacing the organic cation by a Cs+ cation located at the nitrogen position. This has been further verified in the present work for the orthorhombic Pnma phases of $CH_3NH_3PbCl_3$ (fig. S6) and $CH_3NH_3GeCl_3$ (fig. S8). Thus all results are obtained with this procedure expect for figures S6, and S8 for which the $CH_3NH_3^+$ cation was explicitly taken into account.

Moreover, it is well known that the DFT (LDA or GGA) bandgaps are underestimated (38). We have shown in earlier works (17,18) that the nice agreement between DFT bandgaps and values deduced from experiments is fortuitous and stems from error cancellations: both SOC and GW (38) corrections are large and act in opposite directions. Unfortunately, tacking both these effects into account is beyond available computational resources for large systems. Thus, while we believe that the qualitative shape of the reported band structures calculated with SOC should be correct, the reader should keep in mind that GW corrections will not necessarily induce simple rigid shifts over the whole Brillouin zone. Indeed renormalization is expected to be larger at the critical point (e. g. R point in the cubic phase) (38).

Considering two-particle wave function and effective mass equations for electron and hole, optical absorption spectra (fig. S12) have been computed for bound and continuum states (39). The energy and absorption of the excitonic bound states are related to the Rydberg energy of the transition. The absorption of the continuum states is enhanced by the so-called Sommerfeld factor. The whole absorption spectrum was computed for different dielectric constants in order to highlight screening effects.

The energy parameters for the optical matrix elements are obtained for each pair of [CB,VB] states from the expression (26,39): $\frac{2}{m_e}\left|\langle \psi_{CB}| -i\hbar\nabla|\psi_{VB}\rangle\right|^2$. Values given tables S3-S6 take into account the level degeneracies (depicted fig. S1), spin degeneracies and the threefold contribution stemming from the fact that the star of $\mathbf{k}_M$ contains three arms (see symmetry analysis). In the case of the fundamental optical transition these values can be related to the Kane energy (26,39).

All calculations have been performed with experimental crystal structures: $CH_3NH_3PbI_3$ (20,24), $CH_3NH_3PbCl_3$ (40,41), $CH_3NH_3GeCl_3$ (42,43), $CH_3NH_3SnCl_3$ (30-32) and $CH_3NH_3SnBr_3$ (30,31).

Supplementary Text

The symmetry analysis (44) of the electronic states at M and R points of the BZ leads to the interpretation of the SOC induced splitting and optically allowed transitions (fig. S1). The point group of the $\mathbf{k}_R$ (1/2,1/2,1/2) and $\mathbf{k}_M$ (1/2,1/2,0) vectors are O_h and D_{4h}, respectively. Alternative spin-orbitals notations for the $E_{1/2g}$, $F_{3/2g}$, $E_{1/2u}$, $E_{3/2u}$ irreducible representations (IR) at R point may be used (17,44). $E_{1/2g}$, $F_{3/2g}$ IR are respectively associated to combinations of $|1/2,\pm 1/2\rangle_g$ and $|3/2,\pm 1/2\rangle_g$ $|3/2,\pm 3/2\rangle_g$, whereas $E_{1/2u}$, $F_{3/2u}$ IR are respectively associated to combinations of $|1/2,\pm 1/2\rangle_u$ and $|3/2,\pm 1/2\rangle_u$ $|3/2,\pm 3/2\rangle_u$. All the cross products between IR of the CB and VB at R point given in figure S1, contain the T_{1u} vectorial representation, indicating allowed and isotropic transitions. The cross products between IR at M point (fig. S1) contain the E_u vectorial representation, indicating allowed and transverse isotropic transitions (in the (x,y) plane for the $\mathbf{k}_M$ (1/2,1/2,0) vector). Isotropic optical transitions are predicted because the star of the $\mathbf{k}_M$ vector contains three arms: (1/2,1/2,0), (0,1/2,1/2) and (1/2,0,1/2) which all contribute to the observed absorption.

Supplementary Figures

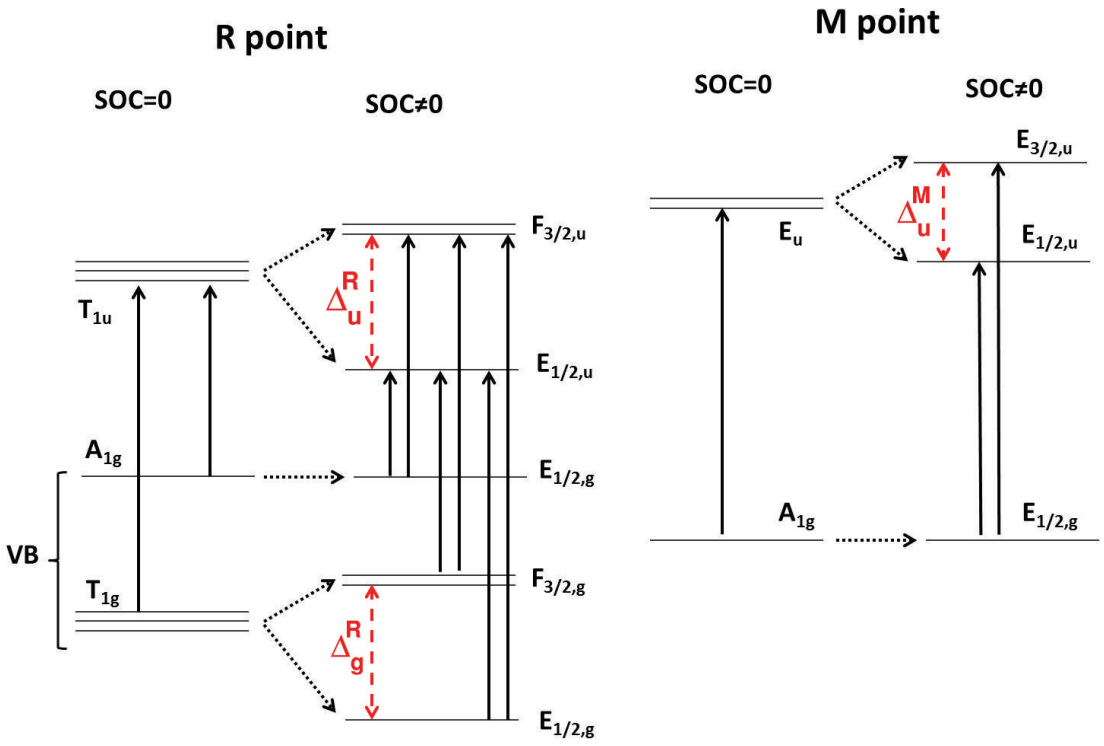

Fig. S1. Schematic energy levels diagrams illustrating the effect of SOC at R and M points of the Pm3m Brillouin zone. Irreducible representations of the simple and double groups at both points are indicated. The level splitting associated to SOC are labeled Δ_g^R, Δ_u^R and Δ_u^M. The additional spin degeneracy is not indicated for the double group representations. The upward arrows show the symmetry allowed optical transitions.

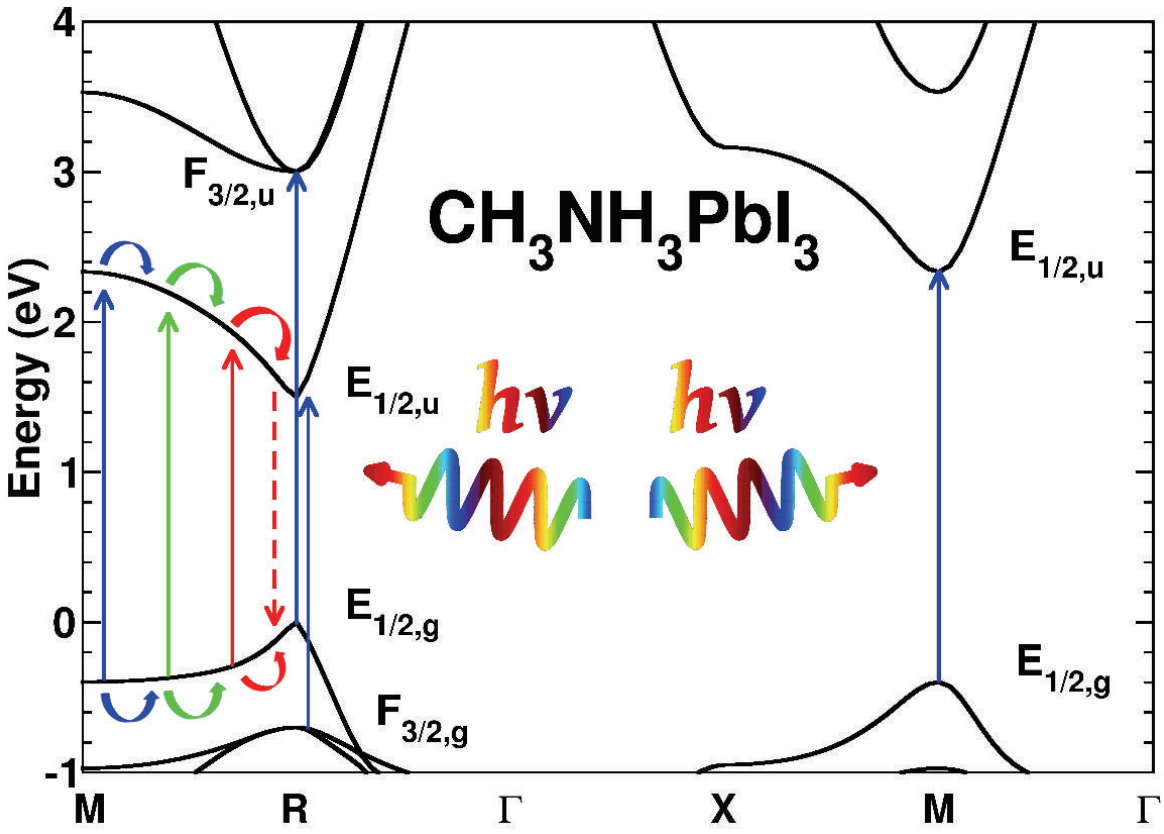

Fig. S2. Electronic band structure for the high temperature cubic Pm3m phase of $CH_3NH_3PbI_3$ with SOC. An upward energy shift of 1.4eV has been applied to match the experimental bandgap value at R.

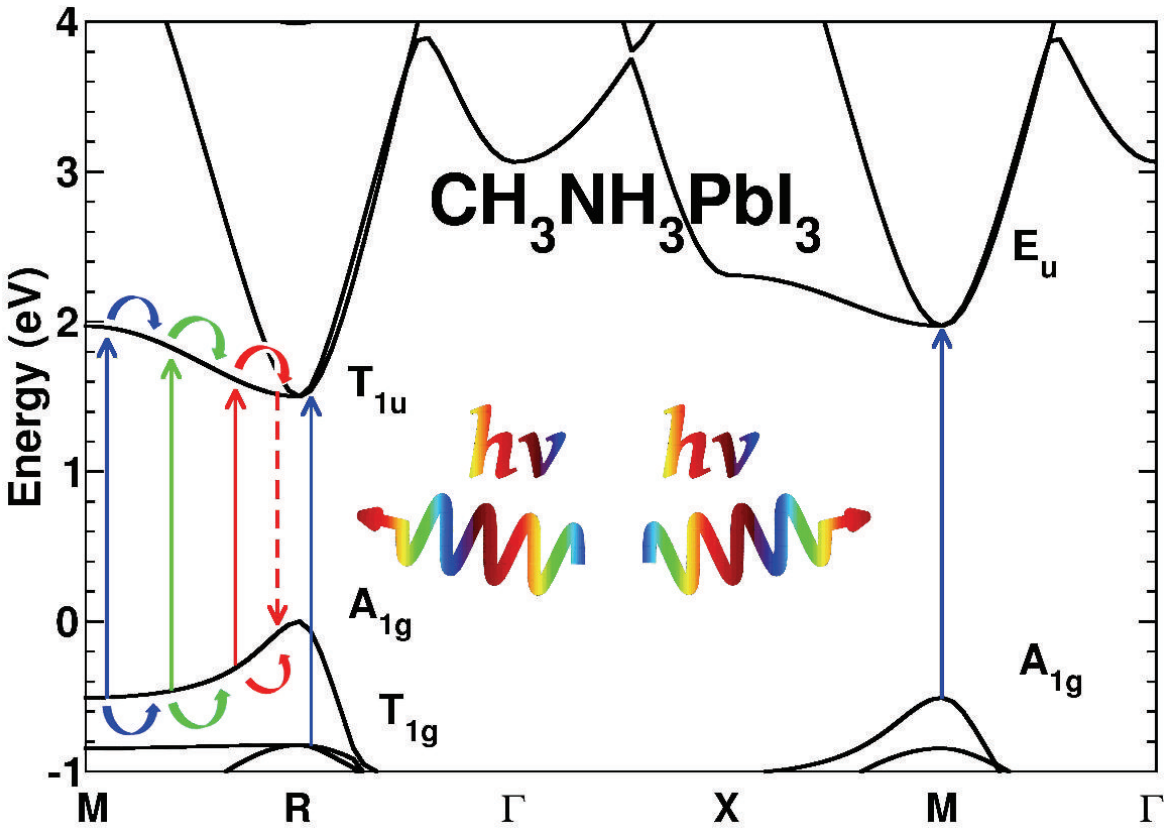

Fig. S3. Electronic band structure for the high temperature cubic Pm3m phase of $CH_3NH_3PbI_3$ without SOC. An upward energy shift of 0.3eV has been applied to match the experimental bandgap value at R.

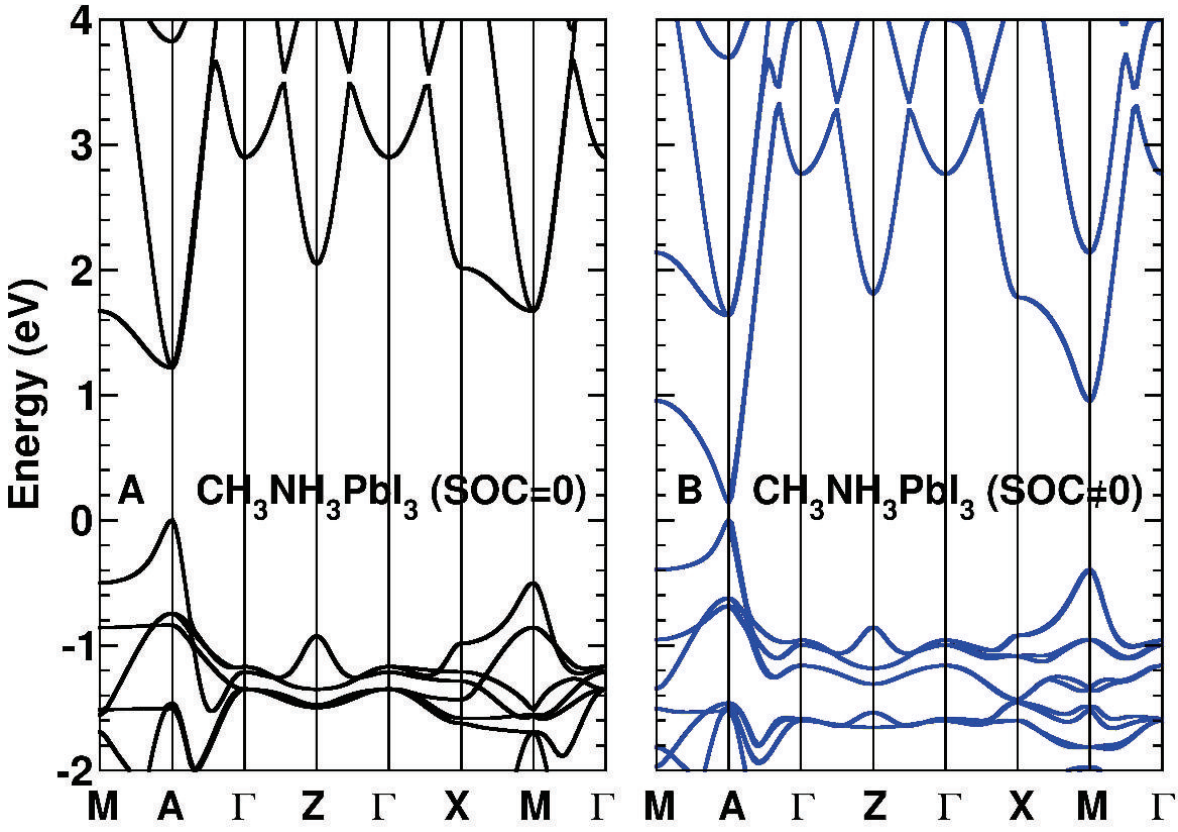

Fig. S4. Electronic band diagrams for the high temperature tetragonal P4mm phase of $CH_3NH_3PbI_3$ without **(A)** and with **(B)** SOC (LDA).

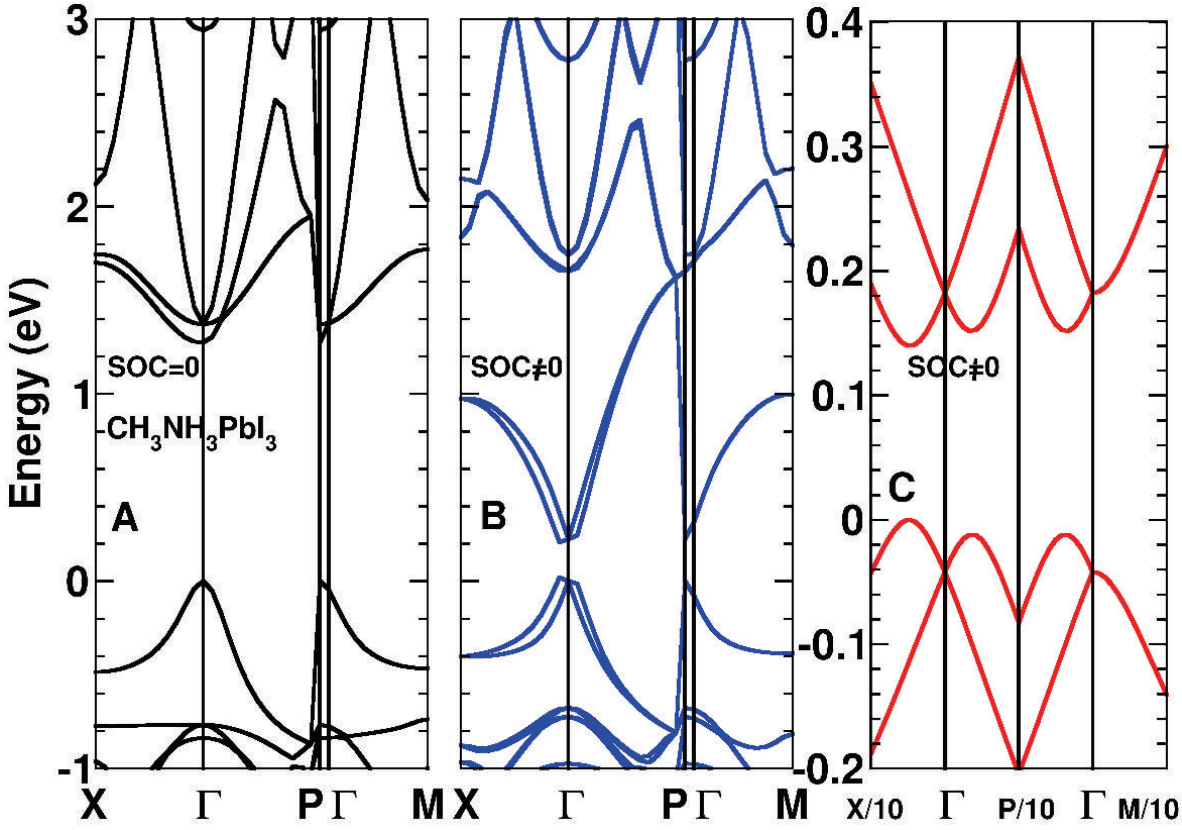

Fig. S5. Electronic band diagrams for the room temperature tetragonal I4mcm phase of $CH_3NH_3PbI_3$ without **(A)** and with **(B)** SOC (LDA). **(C)** Zoom close to the critical point (Γ) revealing the slight splitting due to SOC.

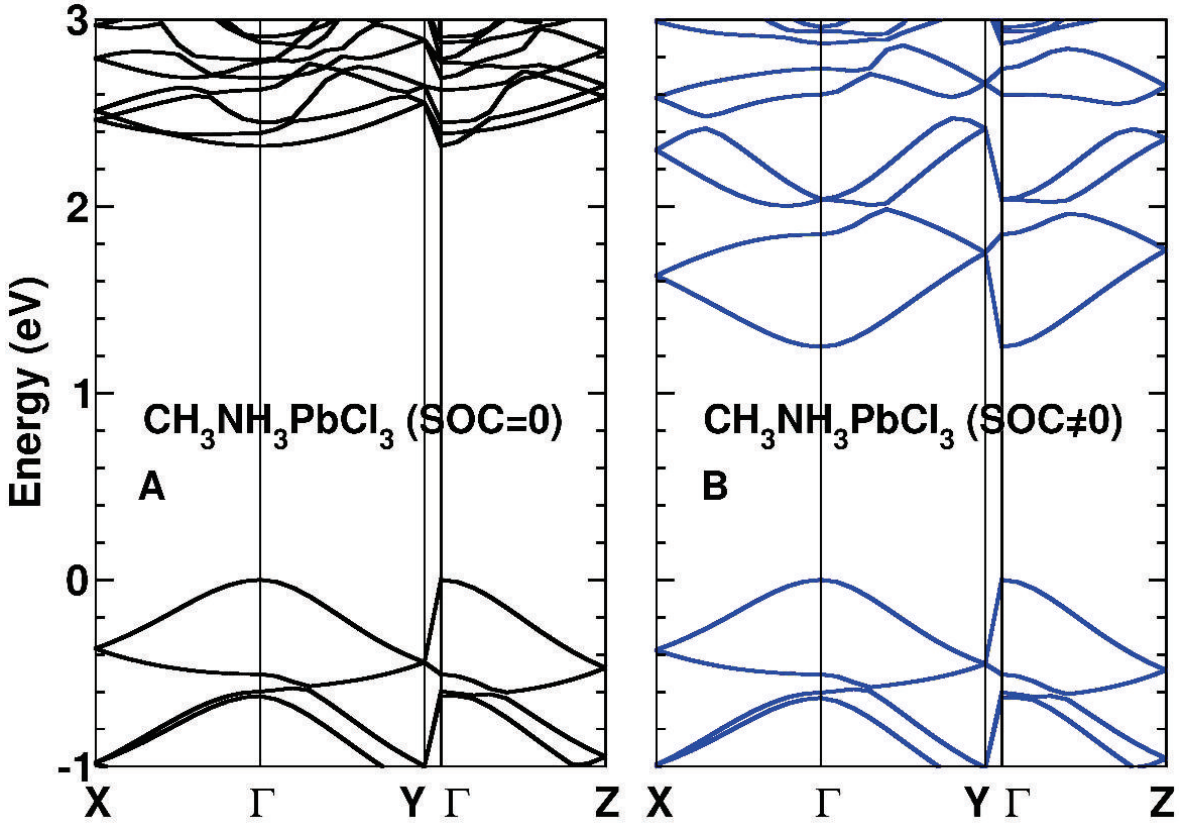

Fig. S6. Electronic band diagrams for the low temperature orthorhombic Pnma phase of $CH_3NH_3PbCl_3$ without **(A)** and with **(B)** SOC (LDA).

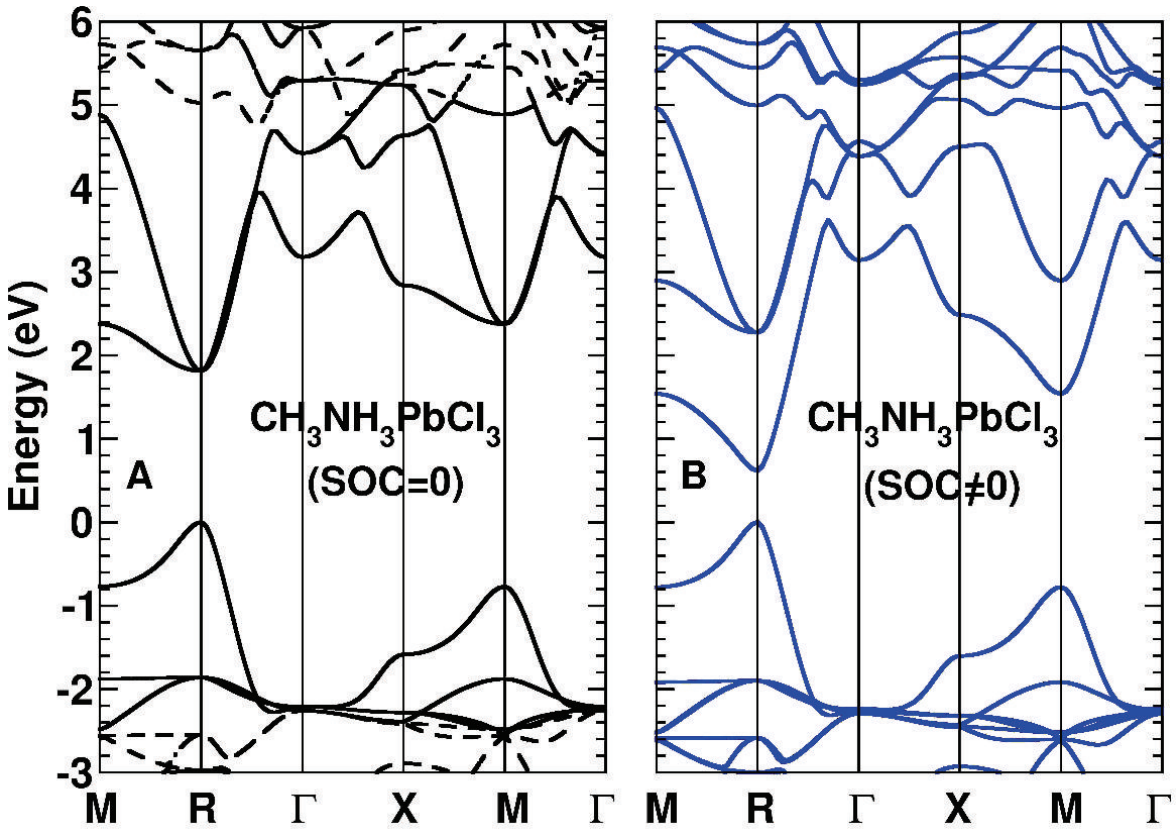

Fig. S7. Electronic band diagrams for the high temperature cubic Pm3m phase of $CH_3NH_3PbCl_3$ without **(A)** and with **(B)** SOC (LDA).

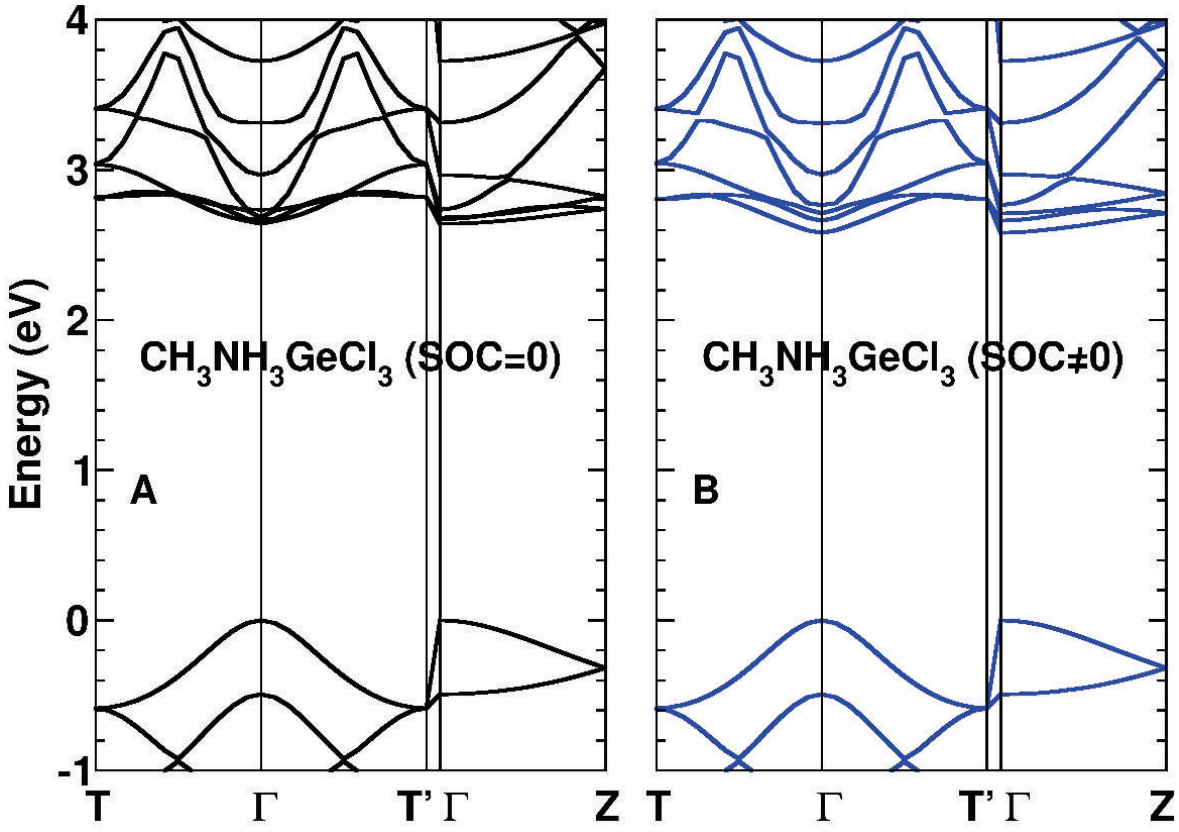

Fig. S8. Electronic band diagrams for the room temperature orthorhombic Pnma phase of $CH_3NH_3GeCl_3$ without **(A)** and with **(B)** SOC (LDA).

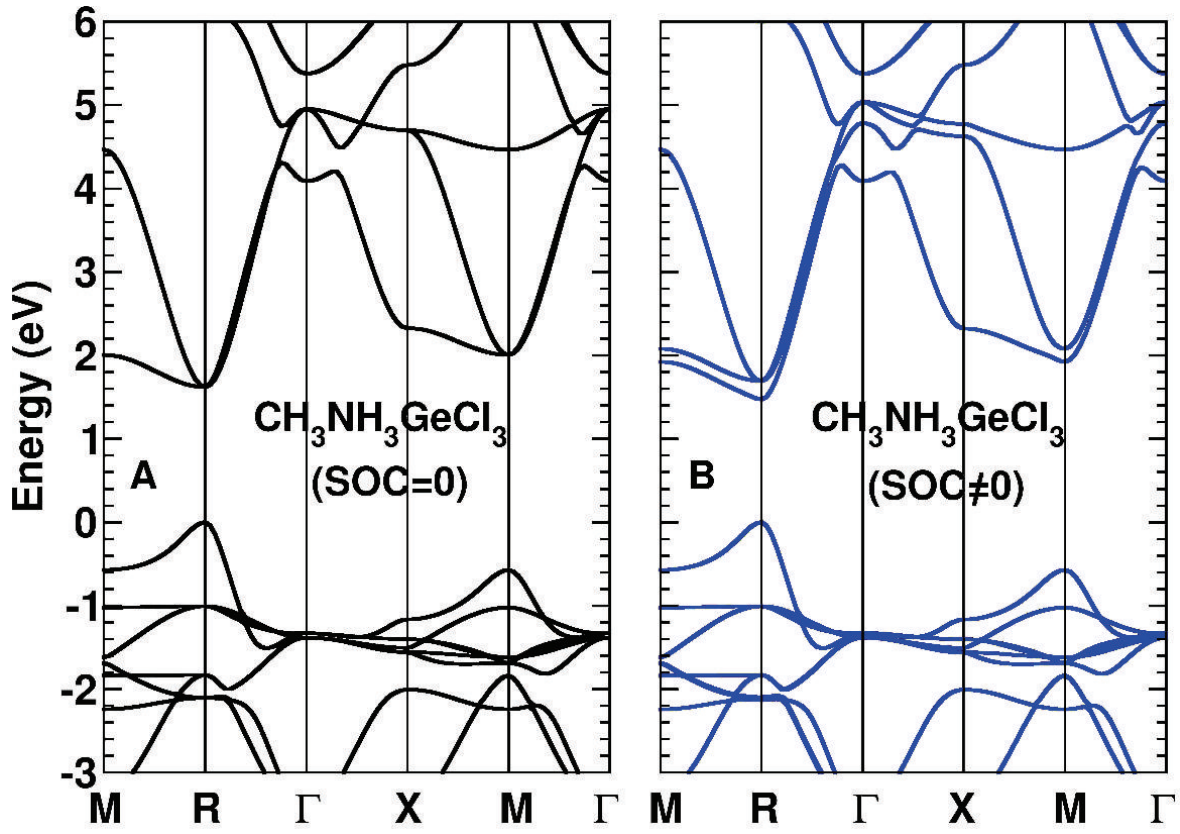

Fig. S9. Electronic band diagrams for the high temperature cubic Pm3m phase of $CH_3NH_3GeCl_3$ without **(A)** and with **(B)** SOC (LDA).

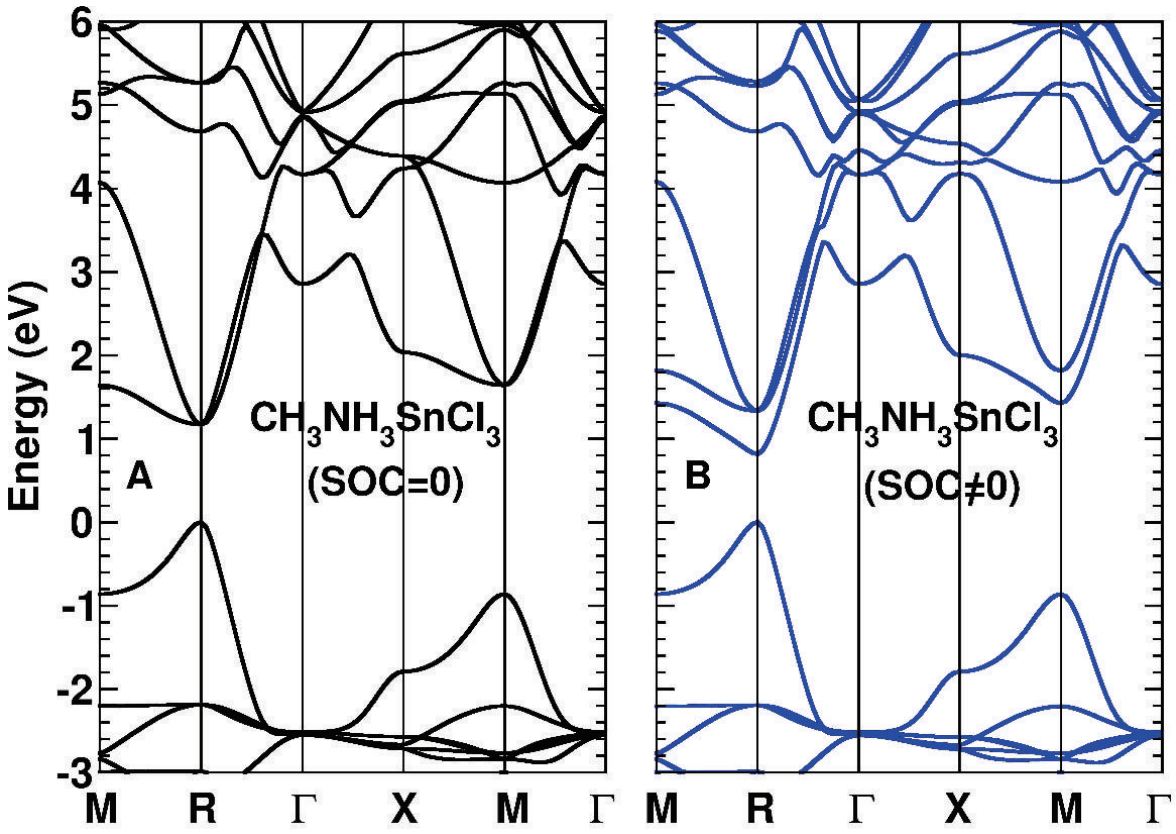

Fig. S10. Electronic band diagrams for the high temperature cubic Pm3m phase of $CH_3NH_3SnCl_3$ without **(A)** and with **(B)** SOC (LDA).

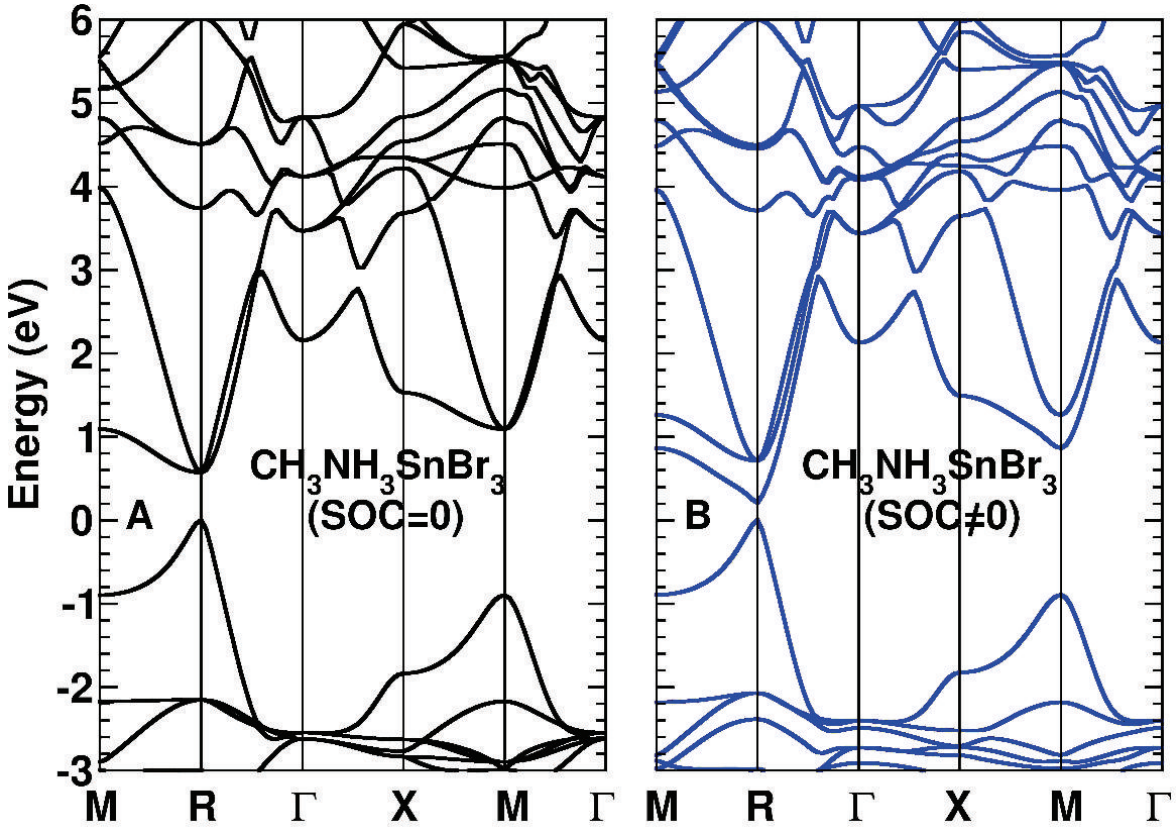

Fig. S11. Electronic band diagrams for the high temperature cubic Pm3m phase of $CH_3NH_3SnBr_3$ without **(A)** and with **(B)** SOC (LDA).

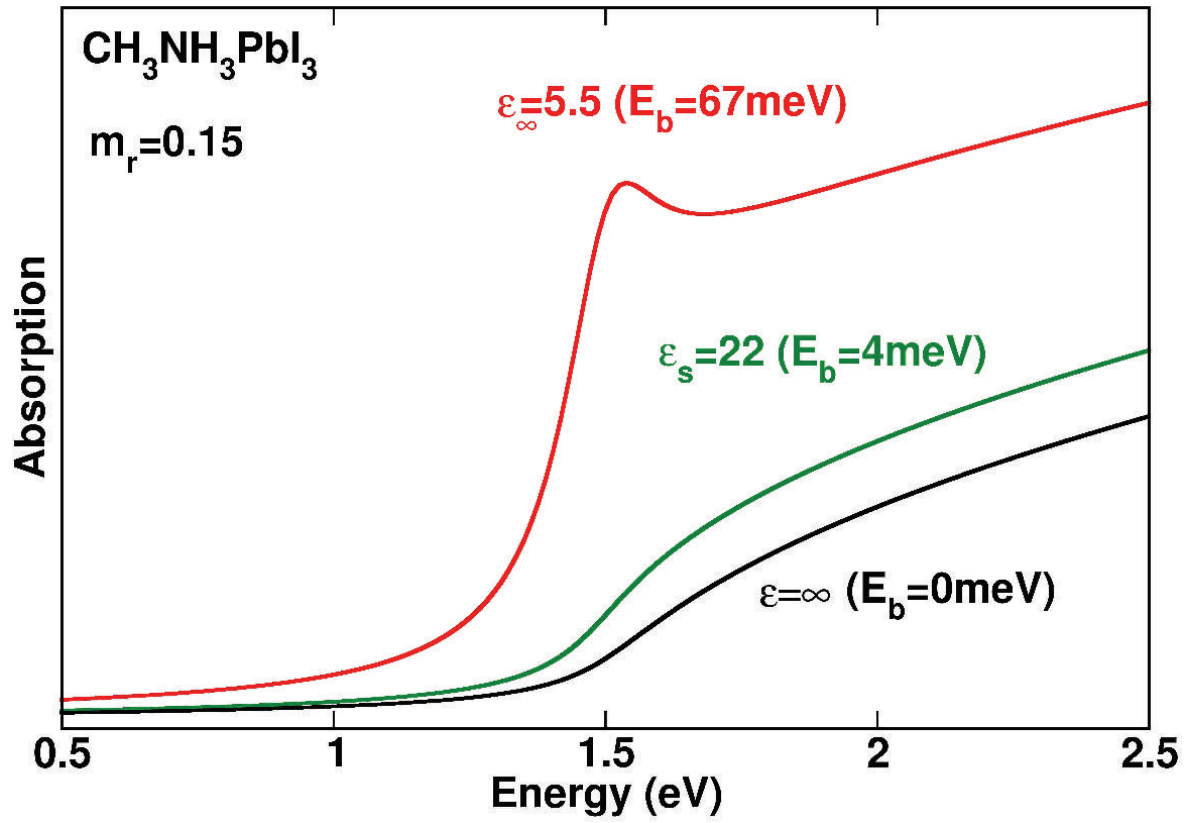

Fig. S12. Optical absorption spectra for the high temperature cubic Pm3m phase of $CH_3NH_3PbI_3$ computed for bound and continuum states, considering two-particle wave function and effective mass equations for electron and hole (39). A damping factor of 0.1eV has been used. Dielectric constants ε_∞ and ε_S have been taken from reference (19).

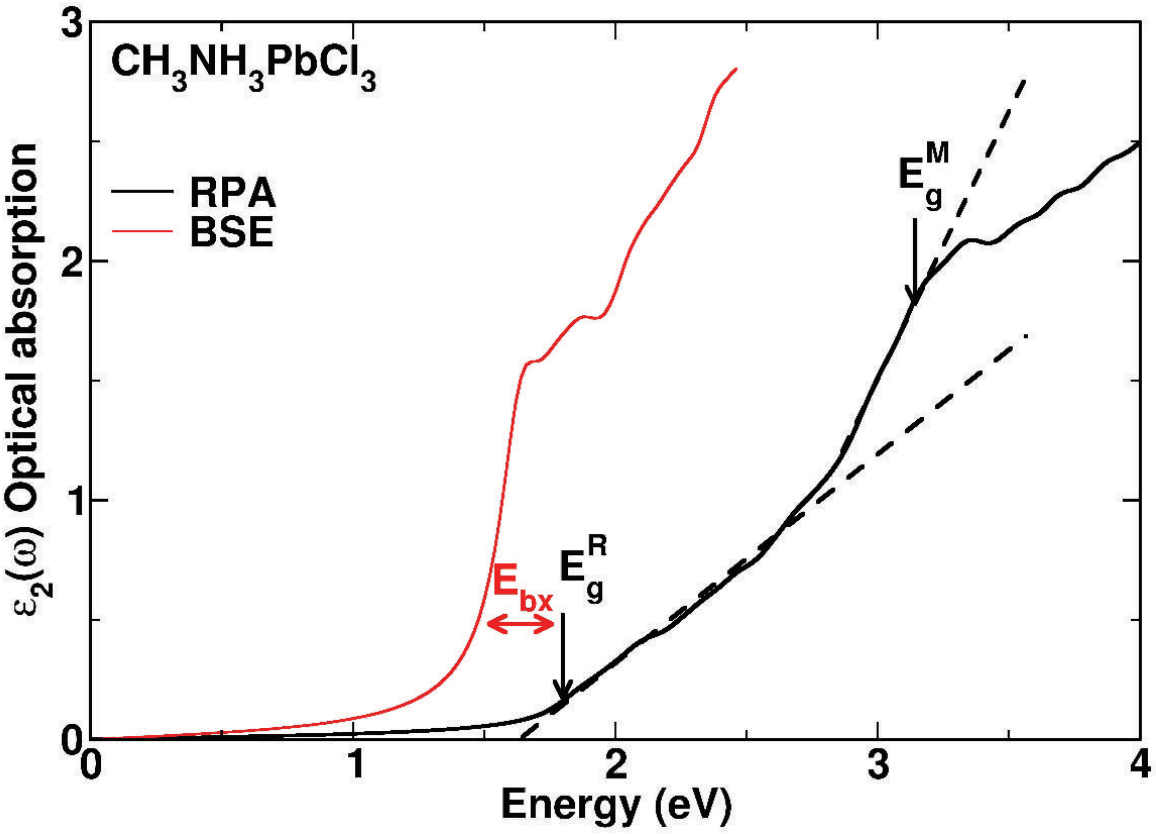

Fig. S13. Optical absorption spectra for the high temperature cubic Pm3m phase of $CH_3NH_3PbCl_3$ with (BSE, red) and without (RPA, black) the excitonic interaction. Onsets of optical transitions at the R (E_g^R) and M (E_g^M) points and exciton binding energy (E_{bx}) are indicated.

Supplementary Tables

Table S1. Comparison between calculated electronic bandgaps for $CH_3NH_3PbX_3$ (X=I, Br, Cl), and optical bandgaps measured at room temperature (RT). Calculated values are reported for the low temperature (LT) orthorhombic Pnma phase and room temperature (RT) cubic Pm3m phase. Values in brackets have been obtained without SOC.

Eg (eV)	X=I	X=Br	X=Cl
LT (GGA)	0.5 (1.5)	0.8 (1.9)	-
LT (LDA)	0.4 (1.4)	- (1.9)	1.2 (2.3)
RT (LDA)	0.2 (1.3)	0.5 (1.5)	0.6 (1.8)
RT (exp.)	1.5 (ref. 4)	2.3 (ref. 4)	3.1 (ref. 29)

Table S2. Comparison between calculated electronic bandgaps for $CH_3NH_3MCl_3$ (M=Pb, Sn, Ge), and optical bandgaps measured at room temperature (RT). For M=Ge,Sn and Pb the room temperature (RT) phases are respectively orthorhombic Pnma, triclinic P1 and cubic Pm3m. For M=Sn and Ge the calculated bandgaps for the high temperature (HT) cubic Pm3m phases are also given. Values in brackets have been obtained without SOC.

Eg (eV)	M=Pb	M=Sn	M=Ge
RT (LDA)	0.6 (1.8)	(*GGA: 2.0*) (ref. 30)	2.6 (2.6)
HT (LDA)	-	1.1 (1.5)	1.8 (1.9)
RT (exp.)	3.1 (ref. 29)	3.7 (ref. 30)	-

Table S3. Energy parameters quantifying the optical matrix elements and transition energies (eV) with respect to the bandgap energy (E_g) for the cubic phase of $CH_3NH_3PbI_3$ calculated at the LDA level of theory without SOC. Energy parameters account for level degeneracies (depicted fig. S1), spin degeneracies and the threefold contribution at M.

Eg (eV)	T_{1u}^{R}	E_{u}^{M}
A_{1g}^{R}	40 (E_g)	0
A_{1g}^{M}	0	120 (E_g+*1.0*)
T_{1g}^{R}	16 (E_g+*0.8*)	0

Table S4. Energy parameters quantifying the optical matrix elements and transition energies (eV) with respect to the bandgap energy (E_g) for the cubic phase of $CH_3NH_3PbI_3$ calculated at the LDA level of theory with SOC. Energy parameters account for level degeneracies (depicted fig. S1), spin degeneracies and the threefold contribution at M.

Eg (eV)	$E_{1/2u}^{R}$	$E_{1/2u}^{M}$	$E_{3/2u}^{R}$
$E_{1/2g}^{R}$	17 (E_g)	0	18 (E_g+*1.6*)
$E_{1/2g}^{M}$	0	60 (E_g+*1.4*)	0
$F_{3/2g}^{R}$	5 (E_g+*0.8*)	0	*10 (E_g+2.4)*

Table S5. Energy parameters quantifying the optical matrix elements and transition energies (eV) with respect to the bandgap energy (E_g) for the cubic phase of $CH_3NH_3PbCl_3$ calculated at the LDA level of theory without SOC. Energy parameters account for level degeneracies (depicted fig. S1), spin degeneracies and the threefold contribution at M.

Eg (eV)	T_{1u}^{R}	E_{u}^{M}
A_{1g}^{R}	38 (E_g)	0
A_{1g}^{M}	0	132 (E_g+*1.3*)
T_{1g}^{R}	26 (E_g+*1.9*)	0

Table S6. Energy parameters quantifying the optical matrix elements and transition energies (eV) with respect to the bandgap energy (E_g) for the cubic phase of $CH_3NH_3PbCl_3$ calculated at the LDA level of theory with SOC. Energy parameters account for level degeneracies (depicted fig. S1), spin degeneracies and the threefold contribution at M.

Eg(eV)	$E_{1/2u}^{R}$	$E_{1/2u}^{M}$	$E_{3/2u}^{R}$
$E_{1/2g}^{R}$	14 (E_g)	0	23 (E_g+*1.7*)
$E_{1/2g}^{M}$	0	63 (E_g+*1.7*)	0
$F_{3/2g}^{R}$	6 (E_g+*1.9*)	0	20 (E_g+4.2)

Supplementary References

1. W. Shockley, H. J. Queisser, Detailed Balance Limit of Efficiency of p-n Junction Solar Cells, *J. Appl. Phys.*, **32**, 510-519 (1961).

2. M. A. Green, K. Emery, Y. Hishikawa, W. Warta, E.D. Dunlop, Solar cell efficiency tables (version 42), *Prog. Photovolt: Res. Appl.*, **21**, 827–837 (2013).

3. D.J. Friedman, Current Opinion in Solid State and Materials Science, *Current Opinion in Solid State and Materials Science*, **14**, 131-138 (2010).

4. A. Kojima, K. Teshima, Y. Shirai, T. Miyasaka, Organometal Halide Perovskites as Visible-Light Sensitizers for Photovoltaic Cells, *J. Am. Chem. Soc.*, **131**, 6050-6051 (2009).

5. M. M. Lee, J. Teuscher, T. Miyasaka, T. N. Murakami, H. J. Snaith, Efficient Hybrid Solar Cells Based on Meso-Superstructured Organometal Halide Perovskites, *Science*, **338**, 643-647 (2012).

6. H-S. Kim, C-R. Lee, J-H Im, K-B. Lee, T. Moehl, A. Marchioro, S-J. Moon, R. Humphry-Baker, J-H. Yum, J. E. Moser, M. Grätzel, N-G. Park, Lead Iodide Perovskite Sensitized All-Solid-State Submicron Thin Film Mesoscopic Solar Cell with Efficiency Exceeding 9%, *Sci. Rep.*, **2**, 591-1-591-7 (2012).

7. J. H. Heo, S. H. Im, J. H. Noh, T.N. Mandal, C.S. Lim, J.A. Chang, Y.H. Lee, H.J. Kim, A. Sarkar, M.K. Nazeeruddin, M. Gratzel, S. I. Seok, Efficient inorganic–organic hybrid heterojunction solar cells containing perovskite compound and polymeric hole conductors, *Nature Photonics*, **7**, 486-491 (2013).

8. J. Burschka, N. Pellet, S.J. Moon, R. Humphry-Baker, P.Gao, M. K. Nazeeruddin, M. Grätzel, Sequential deposition as a route to high-performance perovskite-sensitized solar cells, *Nature*, **499**, 316-319 (2013).

9. H-S Kim, I. Mora-Sero, V. Gonzalez-Pedro, F. Fabregat-Santiago, E. J. Juarez-Perez, N-G Park, J. Bisquert, Mechanism of carrier accumulation in perovskite thin-absorber solar cells, *Nature Comm.*, **4**, 2242 (2013).

10. N. G. Park, Organometal Perovskite Light Absorbers Toward a 20% Efficiency Low-Cost Solid-State Mesoscopic Solar Cell , *J. Phys Chem. Lett.*, **4**, 2423-2429 (2013).

11. J. H. Noh, S. H. Im, J. H. Heo, T. N. Mandal, S. I. Seok, Chemical Management for Colorful, Efficient, and Stable Inorganic–Organic Hybrid Nanostructured Solar Cells, *Nano Lett.*, **13**, 1764-1769 (2013).

12. M. Liu, M. B. Johnston, H. J. Snaith, Efficient planar heterojunction perovskite solar cells by vapour deposition, *Nature*, **501**, 395-398 (2013).

13. H. Snaith, Perovskites: The Emergence of a New Era for Low-Cost, High-Efficiency Solar Cells, *J. Phys Chem. Lett.*, **4**, 3623-3630 (2013).

14. S. D. Stranks, G. E. Eperon, G. Grancini, C. Menelaou, M. J. P. Alcocer, T. Leijtens, L. M. Herz, A. Petrozza, H. J. Snaith, Electron-Hole Diffusion Lengths Exceeding 1 Micrometer in an Organometal Trihalide Perovskite Absorber, *Science*, **342**, 341-344 (2013).

15. G. Xing, N. Mathews, S. Sun, S. S. Lim, Y. M. Lam, M. Grätzel, S. Mhaisalkar, T. C. Sum, Long-Range Balanced Electron- and Hole-Transport Lengths in Organic-Inorganic $CH_3NH_3PbI_3$, *Science*, **342**, 344-347 (2013).

16. M. Antonietta, J. C. Hummelen, Hybrid solar cells: Perovskites under the Sun, *Nature Mater.*, **12**, 1087-1089 (2013).

17. J. Even, L. Pedesseau, J.-M. Jancu, C. Katan, Importance of Spin–Orbit Coupling in Hybrid Organic/Inorganic Perovskites for Photovoltaic Applications, *J. Phys. Chem. Lett.*, **4**, 2999-3005 (2013).

18. J. Even, L. Pedesseau, J.-M. Jancu, C. Katan, DFT and k · p modelling of the phase transitions of lead and tin halide perovskites for photovoltaic cells, *Phys. Status Solidi RRL*, (2013), DOI 10.1002/pssr.201308183

19. F. Brivio, A. B. Walker, A. Walsh, Structural and electronic properties of hybrid perovskites for high-efficiency thin-film photovoltaics from first-principles, *Appl. Phys. Lett. Mat.*, **1**, 042111-1-042111-5 (2013).

20. T. Baikie, Y. Fang, J. M. Kadro, M. Schreyer, F. Wei, S. G. Mhaisalkar, M. Graetzel, T. J. White, Synthesis and crystal chemistry of the hybrid perovskite $(CH_3NH_3)PbI_3$ for solid-state sensitised solar cell applications , *J. Mater. Chem. A*, **1**, 5628-5641 (2013).

21. S. Colella, E. Mosconi, P. Fedeli, A. Listorti, F. Gazza, F. Orlandi, P. Ferro, T. Besagni, A. Rizzo, G. Calestani, G. Gigli, F. De Angelis, R. Mosca, $MAPbI_{3-x}Cl_x$ Mixed Halide Perovskite for Hybrid Solar Cells: The Role of Chloride as Dopant on the Transport and Structural Properties, *Chem. Mater.*, **25**, 4613-4618 (2013).

22. E. Mosconi, A. Amat, Md. K. Nazeeruddin, M. Grätzel, F. De Angelis, First-Principles Modeling of Mixed Halide Organometal Perovskites for Photovoltaic Applications, *J. Phys. Chem. C*, **117**, 13902-13913 (2013).

23. G. Giorgi, J.-I. Fujisawa, H. Segawa, K. Yamashita, Small Photocarrier Effective Masses Featuring Ambipolar Transport in Methylammonium Lead Iodide Perovskite: A Density Functional Analysis, *J. Phys. Chem. Lett.*, **4**, 4213-4216 (2013).

24. C. C. Stoumpos, C. D. Malliakas, M. G. Kanatzidis, Semiconducting Tin and Lead Iodide Perovskites with Organic Cations: Phase Transitions, High Mobilities, and Near-Infrared Photoluminescent Properties, *Inorg. Chem.*, **52**, 9019-9038 (2013).

25. M. Saurat, M. Ritthoff, Photovoltaics and the RoHS Directive, Position Paper, Wuppertal Institute for Climate, Environment and Energy, May 2010

26. J. Even, L. Pedesseau, M.-A. Dupertuis, J.-M. Jancu, C. Katan, Electronic model for self-assembled hybrid organic/perovskite semiconductors: Reverse band edge electronic states ordering and spin-orbit coupling, *Phys. Rev. B*, **86**, 205301-1-205301-4 (2012).

27. R. Ferreira, G. Bastard, Phonon-assisted capture and intradot Auger relaxation in quantum dots, *Appl. Phys. Lett.*, **74**, 2818-2820 (1999).

28. P. Miska, J. Even, X. Marie, O. Dehaese, Electronic structure and carrier dynamics in InAs/InP double-cap quantum dots, *Appl. Phys. Lett.*, **94**, 061916-1-061916-3 (2009).

29. N. Kitazawa, Y. Watanabe, Y. Nakamura, Optical properties of $CH_3NH_3PbX_3$ (X = halogen) and their mixed-halide crystals, *J. Mat. Sci.*, **37**, 3585-3587 (2002).

30. F. Chiarella, A. Zappettini, F. Licci, Combined experimental and theoretical investigation of optical, structural, and electronic properties of $CH_3NH_3SnX_3$ thin films (X=Cl,Br), *Phys. Rev. B*, **77**, 045129-1-045129-6 (2008).

31. K. Yamada, K. Nakada, Y. Takeuchi, K. Nawa, Y.Yamane, Tunable Perovskite Semiconductor $CH_3NH_3SnX_3$ (X: Cl, Br, or I) Characterized by X-ray and DTA, *Bull. Chem. Soc. Jpn*, **84**, 926-932 (2011).

32. K. Yamada, Y. Kuranaga, K. Ueda, S. Goto, T. Okuda, Y. Furukawa, Phase Transition and Electric Conductivity of $ASnCl_3$ (A = Cs and CH_3NH_3), *Bull. Chem. Soc. Jpn.*, **71**, 127-134 (1998).

33. Here we may notice that excitonic effects for the secondary transition at M (fig. 1) are expected to be vanishing as a consequence of its saddle point nature.

34. X. Gonze, J.-M. Beuken, R. Caracas, F. Detraux, M. Fuchs, G.-M. Rignanese, L. Sindic, M. Verstraete, G. Zerah, F. Jollet, M. Torrent, A. Roy, M. Mikami, P. Ghosez, J.-Y. Raty, D. Allan, First-principles computation of material properties: the ABINIT software project, *Comp. Mat. Sci.* **25**, 478-492 (2002).

35. J. P. Perdew, K. Burke, M. Ernzerhof, Generalized Gradient Approximation Made Simple, *Phys. Rev. Lett.* **77**, 3865-3868 (1996).

36. C. Hartwigsen, S. Goedecker, J. Hutter, Relativistic separable dual-space Gaussian pseudopotentials from H to Rn, *Phys. Rev. B*, **58**, 3641-3662 (1998).

37. L. Pedesseau, J-M. Jancu, A. Rolland E. Deleporte, C. Katan, J. Even, Electronic properties of 2D and 3D hybrid organic/inorganic perovskites for optoelectronic and photovoltaic applications, *Opt. Quant. Electron.,* **2013**, doi: 10.1007/s11082-013-9823-9

38. G. Onida, L. Reining, A. Rubio, Electronic excitations: density-functional versus many-body Green's-function approaches, *Rev. Mod. Phys.* **74**, 601-659 (2002).

39. S. Chuang, *Physics of Optoelectronic Devices*, (J. W. Goodman Ed., New York: Wiley, 1995).

40. A. Poglitsch, D. Weber, Dynamic disorder in methylammoniumtrihalogenoplumbates (II) observed by millimeter‐wave spectroscopy , *J. Chem. Phys.*, **87**, 6373-6378 (1987).

41. L. Chi, I. Swainson, L. Cranswicka, J-H Herb, P. Stephens, O. Knop, The ordered phase of methylammonium lead chloride $CH_3ND_3PbCl_3$, *J. Solid State Chem.*, **178**, 1376-1385 (2005).

42. B. R. Serr, G. Heckert, H. W. Rotter, G. Thiele, Structural and spectroscopic studies on trimorphous $MeNH_3GeCl_3$, *J. Mol. Struct.* **348**, 95-98 (1995).

43. K. Yamada, K. Mikawa, T. Okuda, K. S. Knight, Static and dynamic structures of $CD_3ND_3GeCl_3$ studied by TOF high resolution neutron powder diffraction and solid state NMR, *J. Chem. Soc. Dalton Trans.*, 2112-2118 (2002).

44. S. L. Altmann, P. Herzig, Point-Group Theory Tables; (Clarendon Press, Oxford, 1994)